Scaled Atmospheric Blooming Experiments (SABLE)

Daniel G. Fouche, Charles Higgs, and C. Frederick Pearson

The SABLE field experiments investigated the use of phase-conjugate adaptive optics to compensate for strong thermal blooming and turbulence. The experiments, conducted at the TRW Capistrano Test Site in southern California over horizontal paths of 100 and 400 m, were designed to explore issues related to the propagation of high-power lasers from the ground to space. The laser used in the experiments was the 10-kW hydrogen-fluoride (HF) Alpha Verification Module (AVM).

Considerable diagnostic instrumentation was incorporated into SABLE to enable detailed measurements of the characteristics of the beam at both ends of the propagation path, the atmosphere along the path, and the adaptive optics system. The measurements were used both to interpret the experimental results and to test the accuracy of MOLLY, a four-dimensional computer propagation code developed at Lincoln Laboratory.

SABLE demonstrated that (1) phase-conjugate adaptive optics can successfully compensate for severe blooming in the real atmosphere over a wide range of atmospheric conditions, (2) wind variations suppress the phase-compensation instability (PCI) and improve system performance significantly, and (3) the computer propagation code can accurately predict system performance for adaptive optics compensation of turbulence and severe thermal blooming in the real atmosphere.

WHEN A HIGH-POWER LASER BEAM is propagated from the ground to an object in space, the beam must be carefully controlled at the ground to ensure that most of the beam energy arrives at the object. Several phenomena can limit the fraction of laser energy that will be captured. Of great interest and concern is spreading of the beam caused by wavefront distortions incurred during the beam's propagation through the atmosphere. The wavefront distortions introduced by the atmosphere are caused by refractive-index variations over the beam cross section. One source of these variations is optical turbulence, i.e., random temperature fluctuations in the atmosphere. Another source of refractivity variations can arise from absorption of laser beam energy by molecules and aerosols in the atmosphere. Absorption leads to heating of the air within the beam footprint; the heated air becomes less dense and creates a defocusing atmospheric lens. The resulting beam spreading is known as thermal blooming. (Reference 1 describes the phenomenon of thermal blooming in detail.) For the beam sizes and power levels required by most practical applications, thermal blooming and turbulence, if uncompensated, can result in beam spreading that greatly reduces the fraction of energy arriving at the target in space.

Adaptive optics can be used to compensate for turbulence and thermal blooming. In a phase-conjugate adaptive optics system, light from a beacon in the direction of the target in space propagates down through the atmosphere and accumulates phase errors that are induced by blooming and turbulence (as described by D.P. Greenwood et al. in Reference 2). On the ground, a wavefront sensor measures the

accumulated phase errors on the beacon wavefront. A deformable mirror is then adjusted in real time to a shape that gives the outgoing laser beam a wavefront that is conjugate to the distorted beacon wavefront, thus precorrecting the outgoing beam for the distortions it will experience as it propagates through the atmosphere.

Compensation for ground-to-space turbulence has been demonstrated, both for low-power-laser propagation and for astronomical imaging, as described by Greenwood et al. [2] and D.V. Murphy [3]. In the same way, an adaptive optics system can compensate for thermal blooming.

Complications can arise in the presence of thermal blooming. One important complication is positive feedback between the blooming and the adaptive optics servo loop. This phenomenon, known as phase-compensation instability (PCI), is described by J.F. Schonfeld in Reference 4. It is generally believed that PCI will limit the power that can be usefully transmitted from the ground to an object in space. In fact, initial theoretical analyses suggested that the performance of full-scale systems would be seriously degraded by PCI. These early analyses, however, were done with idealizations, such as perfect adaptive optics and uniform wind, that led to overly pessimistic assessments of the strength of PCI. Detailed analyses using more realistic models of the adaptive optics [5] and the atmosphere [6] predicted lower growth rates for PCI.

To explore this issue further, Lincoln Laboratory performed calculations with a four-dimensional (three spatial dimensions and time) computer code that included realistic models for the adaptive optics and wind field (as described by Schonfeld in Reference 4). The code was used extensively to simulate the performance of various proposed high-power laser systems. The results of the simulations suggested that the performance of such systems would be adequate for many applications.

These results had to be verified experimentally before a commitment could be made to the substantial expense of developing a full-scale system. Thus a program consisting of suitably scaled laboratory and field experiments was undertaken. The experiments were designed to explore the physics of compensated high-power propagation and to provide a body of experimental data suitable for evaluating the reliability of the numerical simulations.

The experimental program was conducted by Lincoln Laboratory under sponsorship of the U.S. Army and the Strategic Defense Initiative Organization (SDIO). The initial experiments were performed in the laboratory, and the results were in good agreement both qualitatively and quantitatively with results from numerical simulations, as discussed in detail by B. Johnson in Reference 7. The laboratory experiments, however, were not designed to explore the effects of wind variations that are characteristic of a real atmosphere. Such variations were shown by the computer model and by detailed analyses to have a significant effect on real-system performance.

The exploration of compensated propagation under realistic atmospheric conditions required scaled experiments in the field. Because the applications of interest involved propagation to space, a ground-to-space experiment was the preferred configuration. However, the cost of a vertical-propagation experiment was deemed unaffordable, so a horizontal propagation path was used instead. The horizontal-path experiments are called Scaled Atmospheric Blooming Experiments (SABLE).

SABLE was conducted with the Alpha Verification Module (AVM), a 10-kW hydrogen-fluoride (HF) chemical laser located at the TRW Capistrano Test Site (CTS) in southern California. Although the power of the AVM was orders of magnitude below that envisioned for ground-to-space applications, the AVM wavelengths (multiple lines near 2.9 μm in the mid-infrared range) were strongly absorbed by water vapor and carbon dioxide in the atmosphere. The resulting thermal blooming was strong enough to reach parameter regions of interest for high-power lasers. Figure 1 shows the layout at CTS.

The experiments had three objectives:

1. to demonstrate the successful compensation of blooming with adaptive optics (SABLE remains the only atmospheric-propagation experiment performed with multichannel closed-loop adaptive optics and strong thermal blooming),
2. to observe how variations of the wind along the

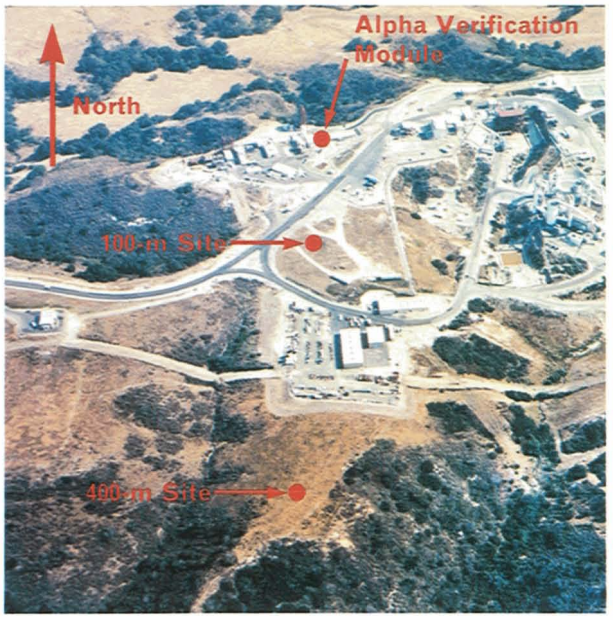

FIGURE 1. Aerial view of Capistrano Test Site in southern California. This photograph was taken before SABLE began. The end points of the 100-m and 400-m propagation paths are shown. The Pacific Ocean is 3 miles off the left (west) side of the photograph.

propagation path affect the correctability of thermal blooming, and

3. to compare the experimental results with predictions of the computer model.

Thorough characterization of the atmosphere and laser beam was an essential feature of SABLE.

In this article, we first describe the physics of the interactions of the laser, the atmosphere, and the adaptive optics system. We then present the design of the experiment, describe the major components of the system, review the computer model, and discuss features specific to SABLE. Finally, we present the experimental results and compare them with predictions of the numerical model.

Physics of Phase Compensation with Strong Thermal Blooming

Electromagnetic radiation in the atmosphere is governed, to a good approximation, by the scalar wave equation. For laser propagation along a particular direction (e.g., the z direction), the governing equation can be further reduced to the paraxial approximation

$$2ikU_z + \Delta_T U + 2k^2 \delta n U = 0,$$

where k is the wave number of the laser, $U(x, y, z, t)$ is the complex wave amplitude, U_z is the partial derivative of U with respect to z, Δ_T is the Laplacian operator in the transverse (x, y) plane, and $\delta n(x, y, z, t)$ is the variation in the index of refraction.

For high-power propagation, δn can depend strongly on the field U, because of laser-induced atmospheric heating. The equation governing the evolution of δn is

$$\delta n_t + (\mathbf{V}_T \cdot \nabla_T)\delta n = -\beta |U|^2,$$

where δn_t is the partial derivative of δn with respect to time, $\mathbf{V}_T$ is the transverse wind vector, ∇_T is the gradient operator in the transverse plane, and $\beta(z)$ depends on atmospheric parameters.

The dependence of δn on $|U|^2$ makes the coupled system fundamentally nonlinear. The strength of the nonlinearity is incorporated into a dimensionless number known as the thermal-blooming distortion number, N_D, given by [1]

$$N_D = \frac{8\sqrt{2}\pi P}{\lambda D} \int_0^L \frac{1}{\rho c_p} \left| \frac{\partial n}{\partial T} \right| \frac{\alpha(z)}{v(z)} H(z) dz,$$

$$\text{where } H(z) = e^{-\int_0^z [\alpha(\xi) + \alpha_s(\xi)] d\xi},$$

and P is the laser power, λ is the beam wavelength, D is the beam diameter, L is the propagation distance, ρ is the mass density, c_p is the specific heat at constant pressure, T is the temperature, α is the absorption coefficient, $v(z)$ is equal to $|\mathbf{V}_T|$, and α_s is the scattering coefficient. N_D depends not only on the laser power but also on the wind-clearing time, which is the time it takes for wind to clear the heated air out of the beam path. (The value of N_D is approximately four times the number of radians of laser-induced wavefront distortion.)

In phase-conjugate adaptive optics, a correction is applied to the outgoing wavefront. The phase at each point on the wavefront is adjusted to negate the cumulative effect of the variations in δn along the beam propagation path. Because the phase is applied at the beginning of the propagation path ($z = 0$), the initial

PHASE COMPENSATION WITH THICK-LENS EFFECTS

AS A WAVEFRONT propagates, modulations in phase will induce modulations in irradiance, and vice versa. This transformation between phase and irradiance causes atmospheric phase aberrations to be manifested as modulations in both phase and irradiance on the beacon wavefront as it reaches the wavefront sensor.

The above effect inherently limits the performance of a phase-conjugate adaptive optics system because only a part of the error on the beacon wavefront—the phase error—is corrected; i.e., no correction for the amplitude variation developed during atmospheric propagation is applied. Not surprisingly, the phase correction alone can not perfectly compensate for the effects of atmospheric inhomogeneities, even with the use of perfect hardware.

The transformation between phase and irradiance becomes more pronounced as the wavefront propagates away from the source of a perturbation (phase or irradiance). An approximate measure of the propagation distance at which these effects become important is $L_0 = \pi d^2/\lambda$, where d is a characteristic dimension of the perturbation and λ is the laser wavelength. The ratio of L_0 to the actual distance L of the perturbation from an observer is defined as the perturbation Fresnel number, $N_P = \pi d^2/(\lambda L)$. Smaller values of N_P indicate a greater degree of interchange between irradiance and phase, and hence a less favorable operational domain for phase-conjugate adaptive optics systems. These small-N_P effects are referred to as thick-lens effects.

In the atmosphere, phase aberrations are in general distributed along the propagation path, rather than concentrated at a particular location. If thermal-blooming effects dominate the effects of optical turbulence, as was the case for SABLE, the length L may be defined as the distance to the centroid of the blooming phase distribution along the propagation path. In this case, we refer to L as the thickness of the blooming layer.

Figure A(1) shows the evolution of an initially plane wavefront from a beacon as its radiation passes through a sinusoidal variation in refractive index at some distance from the transmitter. Figure A(2) shows the evolution of an outgoing wave that has left the transmitter with the conjugate of the beacon phase measured there. The limitations of phase-only compensation can be seen at the top of Figure A(2): after passing through the heated region of the atmosphere, the outgoing wave does not have a flat phase or irradiance.

condition on U is

$$U(\mathbf{x}, 0) = U_o(\mathbf{x})e^{i\phi(\mathbf{x})},$$

where $\mathbf{x}$ is the position in the transverse plane, $U_o(\mathbf{x})$ is the complex amplitude of the outgoing laser beam, and $\phi(\mathbf{x})$ is the phase applied by the adaptive optics system.

For a number of reasons, phase conjugation will not result in perfect compensation. One limitation, for example, is the fitting error caused by approximating a continuous aberration with a mirror surface driven by a finite number of actuators. Errors also arise from sensor noise and limited system bandwidth [3]. In principle, such engineering errors can be reduced to insignificance by the use of better hardware. Nonetheless, phase-conjugate adaptive optics compensation can still be imperfect for a fundamental reason—the wavefront of a beam transforms as it propagates. When significant transformation occurs within the blooming layer, we say that the atmo-

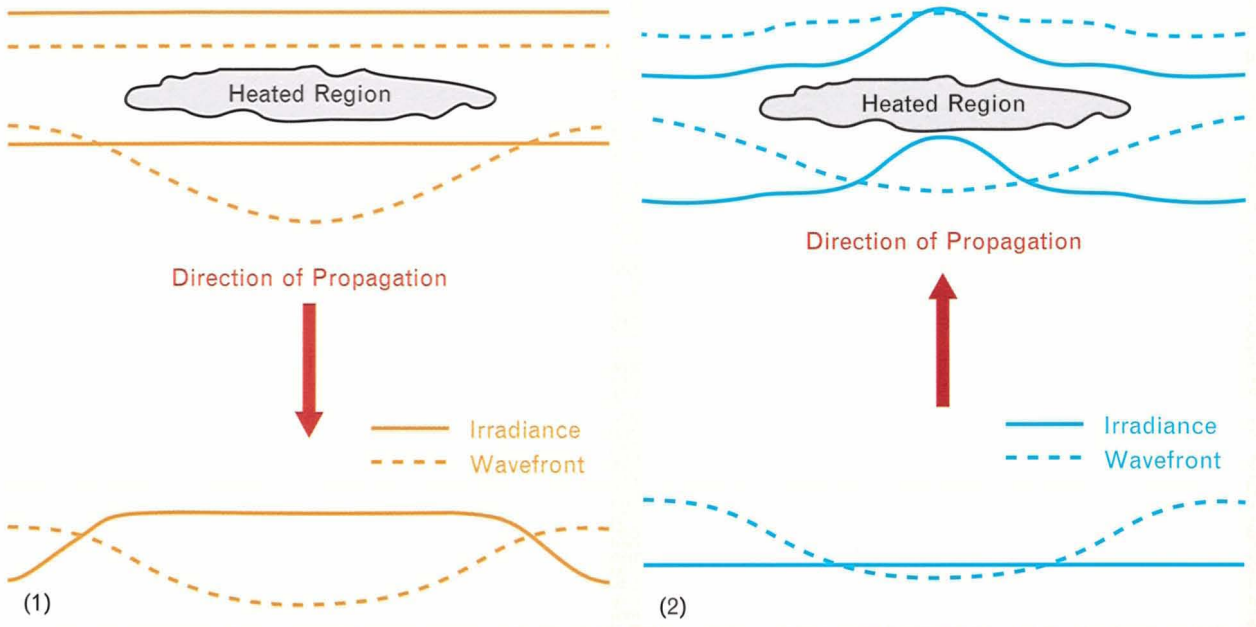

FIGURE A. Phase compensation at small Fresnel number, N_P. A sinusoidal phase disturbance with period $2d$ and amplitude 1 radian is applied at a distance L from the wavefront sensor. The incoming and outgoing waves have the same wavelength λ, and $N_P = \pi d^2/(\lambda L) = 5$. The irradiance level and wavefront position are drawn as increasing in the direction of propagation (down in part *1* and up in part *2*). (1) A beacon with an initial plane wave propagates from the top of the figure to the bottom, and encounters a parcel of heated air (i.e., a hot spot). Because warmer air has a lower index of refraction (a higher speed of propagation for light), the portion of the wavefront in the heated region advances more rapidly. The beacon propagates an additional distance L before reaching the wavefront sensor. At the wavefront sensor, the beacon has developed modulations in both phase and irradiance. (2) A phase-corrected beam propagates in the reverse direction, from bottom to top. Initially, the wavefront of the outgoing beam is the negative of that measured on the beacon, but the irradiance is uniform. The outgoing wavefront propagates to and through the original disturbance. Imperfect correction is seen in the residual phase and irradiance errors on the outgoing beacon after it has propagated through the disturbance. Note the increased irradiance in the region of the heated air; for a high-power outgoing beam, this increase will cause an additional relative heating of the already hot region. The additional heating can lead to a feedback instability, called phase-compensation instability (PCI), which is discussed in the main text.

sphere acts as a thick lens (see the box, "Phase Compensation with Thick-Lens Effects").

A thick lens caused by thermal blooming can be the source of an adaptive optics feedback instability. For example, suppose that the atmosphere far from the transmitter has a small hot spot caused by natural temperature turbulence. The portion of the beacon beam that passes through the hot spot will diverge. The adaptive optics system will sense the divergence and try to compensate by focusing the corresponding portion of the high-power beam. Unfortunately, the focusing will increase the power density at the hot spot, which will then get even hotter as it absorbs more laser power. This process thus involves positive feedback and is clearly unstable. We can see that positive feedback will occur in the example shown in Figure A in the box, "Phase Compensation with Thick-Lens Effects": the irradiance increases at those locations where the sinusoidal wavefront tends to focus the beam.

The positive-feedback process is called phase-compensation instability (PCI). PCI is stronger at higher levels of blooming (higher N_D) and with thicker atmospheric lenses (smaller N_P; see the box, "Phase Compensation with Thick-Lens Effects"). In fact, linearized perturbation theory [8] predicts exponential growth with a rate proportional to N_D/N_P. Because smaller-scale perturbations have smaller values of N_P, they have a higher PCI growth rate. The smallest scale that is reinforced by the adaptive optics is the Nyquist frequency, which is twice the actuator spacing of the deformable mirror. If a perturbation exists at this scale, it will grow fastest. Thus the scale length d chosen for N_P is usually the actuator spacing.

Positive feedback can continue until the hot spots are convected out of the beam by the wind. (Thermal diffusion will also eventually stabilize the process, but generally on a much longer time scale.) Thus the wind-clearing time determines the approximate time scale during which important time-dependent effects occur.

Variations in the wind field along the propagation path play a crucial role in adaptive optics compensation for blooming. A hot spot in the beam (caused, for example, by the local focusing designed to correct for a hot spot in the atmosphere) will create a long filament of heated air along the propagation direction. The phase differences along the filament are all the same sign, which potentially leads to a substantial total phase aberration associated with the filament. If the crosswind is uniform, this coherent addition along the filament will continue until the filament is swept out of the beam. Large phase differences, or gradients, degrade system performance in two ways. First, the deformable mirrors cannot fit the wavefront as accurately, and second, wavefront transformation and PCI are enhanced. But if the crosswind is not uniform in either speed or direction, the filament will break up quickly, so that coherent addition will no longer take place. Consequently, variations in the wind field along the propagation path lead to better system performance.

The wind-variation level σ_v is defined as the square root of the sum of the spatial variances of the wind components perpendicular to the laser propagation direction, normalized by the path-averaged wind speed. As σ_v increases, the deleterious effects of large phase gradients are lessened.

Experimental Approach

A schematic of the experimental arrangement for SABLE is shown in Figure 2. At the transmitter, the output of the AVM laser was expanded to match the size of the active area of the deformable mirrors. After reflecting off a dichroic beam splitter and two deformable mirrors, the beam was expanded further to a size suitable for propagation over the selected range. Once outside the building, the beam propagated through the atmosphere and experienced the effects of thermal blooming and turbulence. The entrance window at the receiver trailer reflected 98% of the laser power into a ground dump; the transmitted 2% provided samples for the diagnostic instruments.

The beacon beam propagated in reverse through the same blooming and turbulence distortions and reflected off the deformable mirrors. After being removed from the common path by a beam splitter, the beacon entered a wavefront sensor, which measured the beam's phasefront. Control electronics adjusted the surfaces of the deformable mirrors to flatten the phasefront of the beacon at the wavefront sensor, thereby precorrecting the AVM beam for the atmospheric distortions.

The SABLE experiments used considerable diagnostic instrumentation. Equipment alongside the propagation path recorded meteorological conditions with good temporal and spatial resolution. Relevant characteristics of the beacon and AVM beams, both at the transmitter and receiver, were also measured with good resolution. Signals from the control electronics, such as servo error and drive voltages to the deformable mirrors, were recorded. With all this information, we could not only obtain quantitative data on the performance of the adaptive optics system under different conditions, we could also perform subsequent computer simulations and compare the results with experimental data.

The SABLE experiments were conducted in two major phases. The first phase was designed to create thick-lens conditions conducive to the excitation of strong PCI. To this end, a small beam size (8×12 cm) was used to make N_D high (up to 500) and N_P low

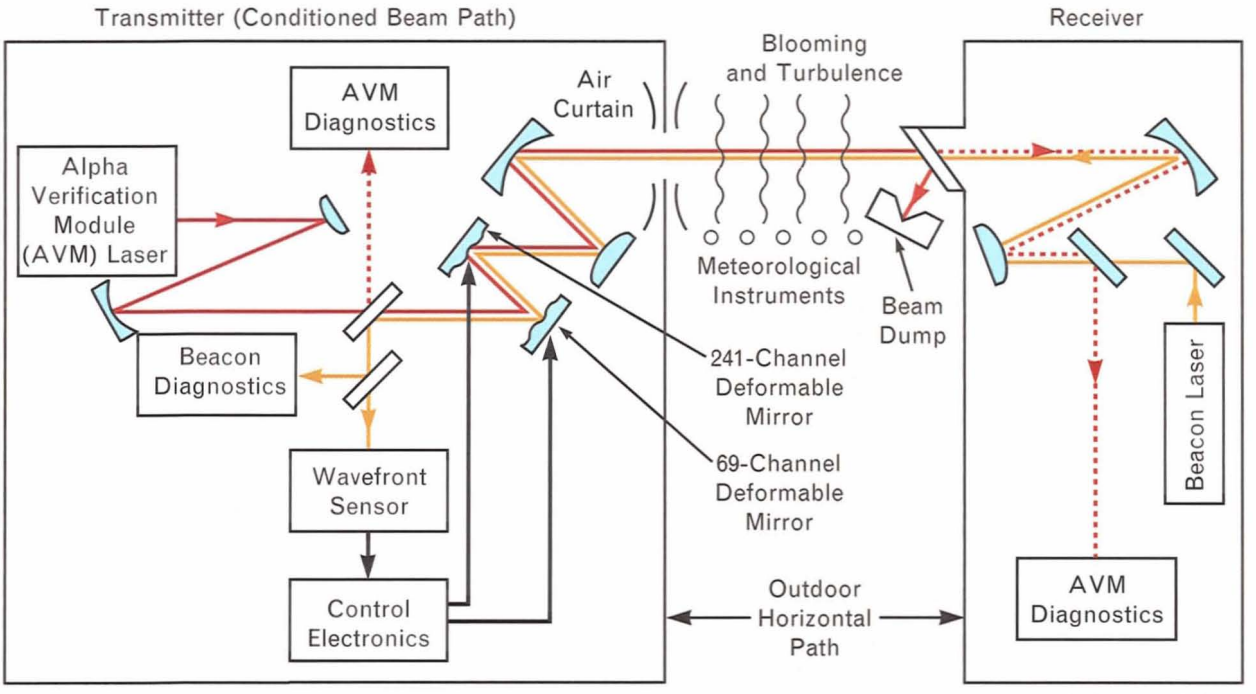

FIGURE 2. Experimental setup for SABLE. The beam from the high-power Alpha Verification Module (AVM) laser is shown in red; the beam from the beacon is shown in tan.

(down to 2). Also, the path was kept relatively short (100 m) to minimize the effects of wind variation. Because of the short path, optical turbulence was relatively unimportant.

In the second phase of the experiments, a longer path (400 m) and larger beam size (18 × 27 cm) were used. Although N_P was larger than in the first phase, PCI was still expected to occur in the absence of wind variations. The longer path was chosen so that there would be considerable wind variation within the blooming layer, providing a good opportunity for PCI mitigation. Although the longer path and larger beam diameter would have allowed stronger effects from optical turbulence, it turned out that most of the 400-m experiments were conducted in the evening, when optical turbulence was not a significant factor.

We conducted many tests for both the 100-m and 400-m phases and anticipated that natural variations in atmospheric conditions from test to test would provide a wide range of values for N_D, N_P, and σ_v. Moreover, within a single laser run, the laser power (and hence N_D) was changed by inserting different attenuators into the beam before it entered the atmosphere. In every lasing test, an attenuator that transmitted only 2% of the full power (thus making blooming insignificant) was used to provide a no-blooming reference condition. Figure 3 and Table 1 summarize the range of parameters that was covered during SABLE.

We used two different modes of adaptive optics operation. For the *ab initio* mode, the adaptive optics system was turned on at the start of high-power propagation, as would be done for an operational laser system. In the *deferred* mode, the adaptive optics system was not turned on until the uncorrected blooming had developed fully.

The deferred mode allowed us to isolate feedback effects. For example, the far-field irradiance just after the adaptive optics system is turned on (but before PCI has had time to become established) indicates system performance in the absence of feedback effects. This performance is limited by such factors as deformable-mirror fitting error and thick-lens effects. The decay in far-field irradiance from the time the adaptive optics system is turned on to a few wind-clearing times later indicates the additional

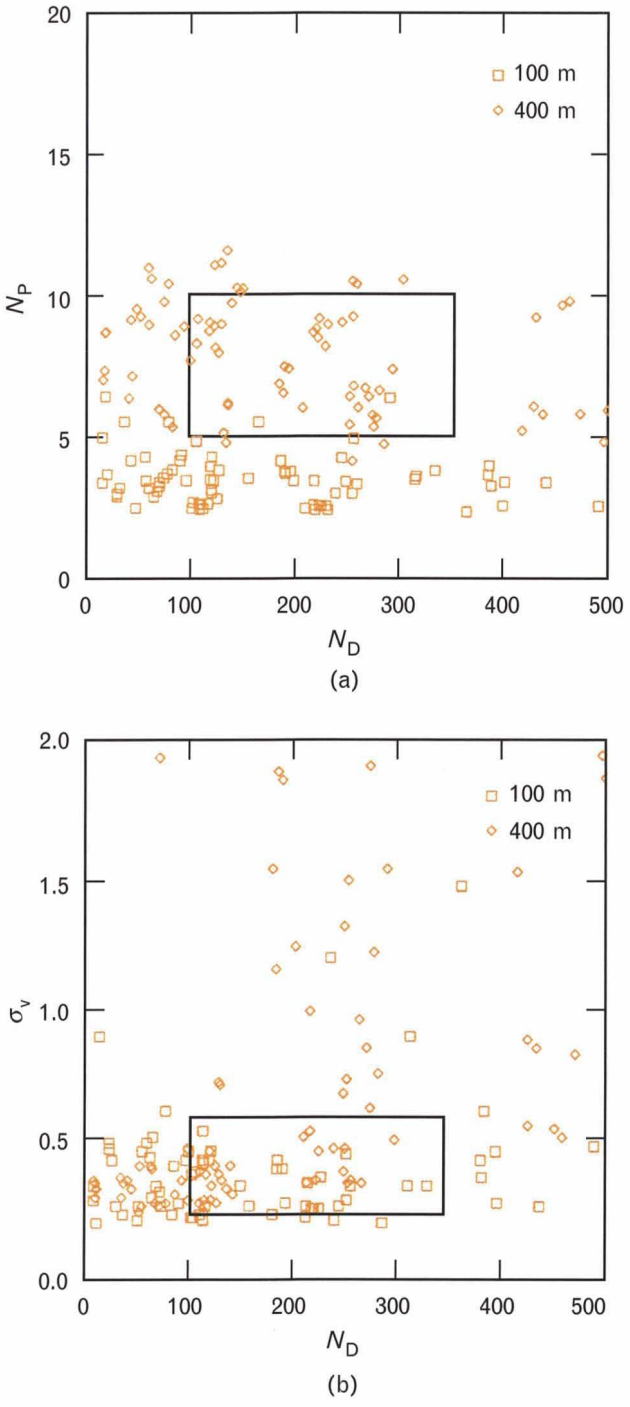

FIGURE 3. Scatter plots of parameter ranges for SABLE 100-m and 400-m tests: (a) perturbation Fresnel number N_P versus thermal-blooming distortion number N_D, and (b) wind variability σ_v versus N_D. The boxes enclose the nominal parameters depicting the strong thermal-blooming regime of interest to our sponsors. Adaptive optics compensation is more difficult for higher thermal-blooming distortion numbers, lower perturbation Fresnel numbers, and lower wind variability.

degradation caused by PCI.

In a typical time line for a laser run, the laser power was sequenced through four levels by means of the attenuators. At each power level, experiments in both deferred and ab initio modes were conducted. A fast shutter in front of the laser was closed for several wind-clearing times during each change of mode and laser power.

Description of Experimental Systems

The following subsections describe the major components of SABLE.

Alpha Verification Module (AVM)

The Alpha Verification Module (AVM) was built by TRW in the early 1980s to verify HF-laser technology. Early in the SABLE program, the spectrum of the AVM beam was measured with a standard resonator in place. The spectrum turned out to be concentrated in lines that are very highly absorbed in the atmosphere. Such high absorption would have caused most of the blooming to occur near the transmitter building. Thin-lens (instead of the desired thick-lens) blooming would have resulted. Consequently, TRW designed and fabricated a new resonator [9] that shifted the spectral distribution to a region of lower absorption. The shift resulted in thick-lens blooming under most atmospheric conditions. The new resonator provided other benefits as well: the irradiance of each spectral line was more uniformly distributed, and the line-to-line variations in the irradiance distribution were reduced. Figure 4 shows the measured all-line irradiance and phase distributions for the laser beam used in SABLE.

Beam-Path Conditioning System

The beam path in the transmitter building was conditioned to minimize unwanted aberrations. Between the laser and the optical bench, the AVM beam propagated through an evacuated pipe, and, after exiting vacuum through a low-distortion window, the beam propagated through dry nitrogen gas (Figure 5). The beam exited the transmitter building through a dual-jet gas curtain (dry nitrogen on one side and outdoor air on the other) that minimized the turbulent-mixing zone at the indoor-outdoor interface.

Table 1. Parameters for SABLE

		Propagation Path	
		100 m	400 m
Beam size	D	8 cm × 12 cm	18 cm × 27 cm
Equivalent actuator spacing*		1 cm	2.2 cm
Beam wavelength	λ	2.9 μm	2.9 μm
Thermal-blooming distortion number	N_D	5–500	1–500
Perturbation Fresnel number	N_p	2–6	4–11
Wind variation level	σ_v	0.2–1.4	0.3–1.8

*The equivalent actuator spacing is the projection of the deformable-mirror actuator spacing on the beam at the transmitting aperture.

Adaptive Optics System

The SABLE adaptive optics system utilized two liquid-cooled deformable mirrors that were used in tandem and separated by a few feet in the optical train. Both mirrors were built for earlier Department of Defense programs and were made available for SABLE. The High-Power Closed-Loop Adaptive System (HICLAS) mirror, built by United Technologies Research Center, has 69 actuators. The peak-to-peak stroke of an ac-

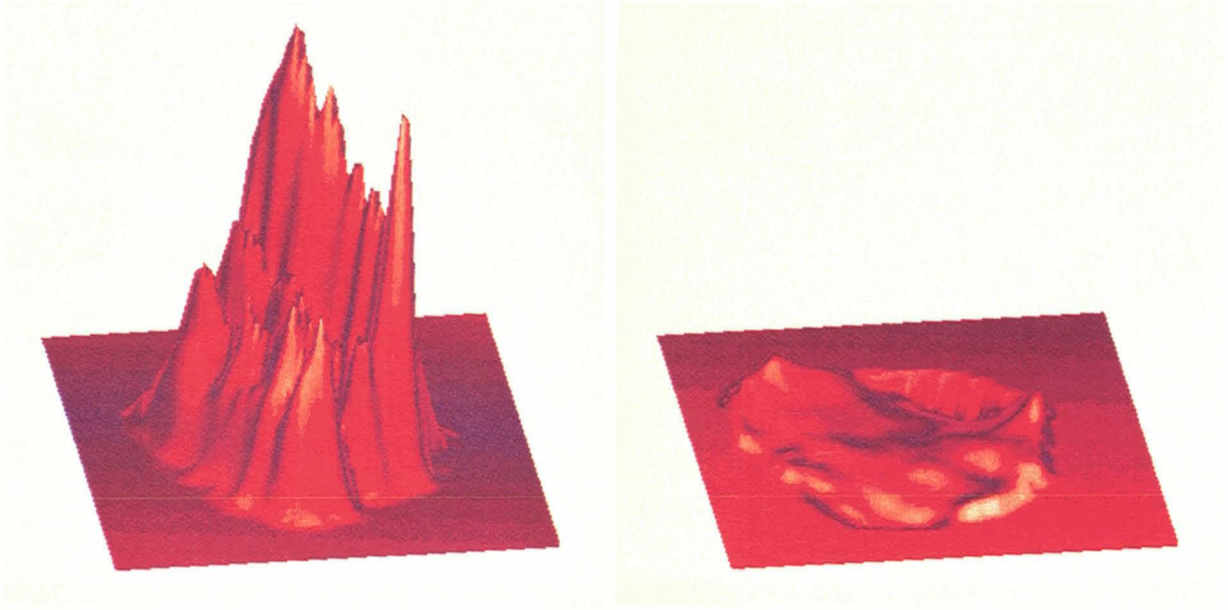

FIGURE 4. AVM beam: measured (left) irradiance and (right) phase distributions. The irradiance distribution is for all spectral lines together; individual spectral lines have similar distributions. The major ridges and valleys in the irradiance distribution are caused by diffraction from edges of mirrors in the resonator. The phase has a 0.2-wave root-mean-square deviation from flat, caused mainly by beam-induced heating of the uncooled optics.

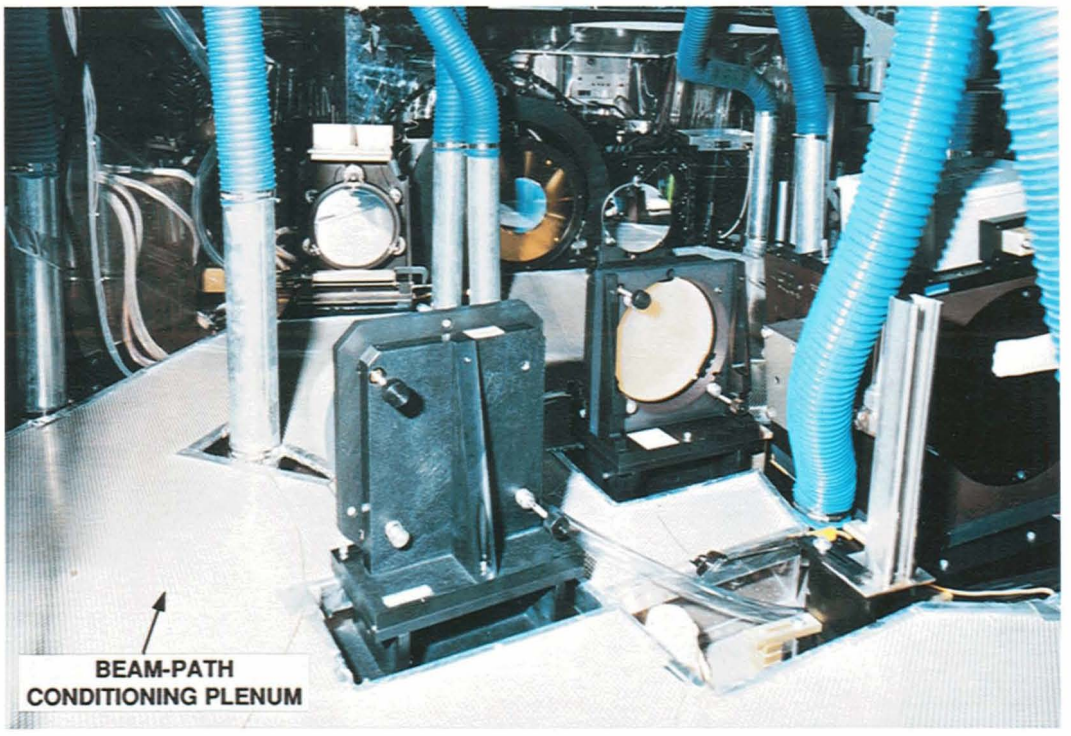

FIGURE 5. View of optical train in transmitter building. Underneath the beam path is the plenum of the beam-path conditioning system. Dry nitrogen gas flows through the diffusing screen covering the plenum and up through the beam path. For minimizing optical turbulence, the gas temperature is carefully maintained to be the same as the temperature of the optical bench. The mirror with the gold bezel near the center of the photograph is the 241-actuator liquid-cooled deformable mirror.

Table 2. Measurements of Beam Characteristics

Device	*Spatial Resolution*	*Temporal Resolution*	*Characteristics Measured**
Pt:Si CCD camera	64 × 64 pixels	480 frames/sec	Alpha Verification Module (AVM) far-field irradiance (T, R)
Pt:Si CCD camera	160 × 122 pixels	60 frames/sec	AVM near-field irradiance (T, R)
InSb CMOS camera	128 × 128 pixels	100 frames/sec	AVM phasefront (R)
Si CCD camera	64 × 64 pixels	480 frames/sec	Beacon far-field irradiance
Si CCD camera (in wavefront sensor)	64 × 64 pixels	480 frames/sec	Beacon phasefront
Reticon camera	128 × 128 pixels	100 frames/sec	Beacon near-field irradiance (after deformable mirror)
Calorimeter	—	1 Hz	AVM power (T)
Scanning spectrometer	—	800 frames/sec	AVM spectrum (T)

*T = at transmitter and R = at receiver

tuator is 18 μm. The other mirror, the Liquid-Cooled Deformable Mirror (LCDM), built by Itek, has 241 active actuators. The LCDM stroke is 4 μm. The actuator spacing of HICLAS is exactly twice that of LCDM, so that the actuator patterns overlay each other. The active area of both mirrors is a 15-cm-diameter circle.

The high-power beam splitter was a sapphire window with a dichroic coating. It reflected the AVM beam and transmitted the beacon beam.

The Hartmann wavefront sensor was built by Lincoln Laboratory. Similar in many respects to the Short-Wavelength Adaptive Techniques (SWAT) wavefront sensor discussed in detail by H.T. Barclay et al. in Reference 10, the SABLE sensor used a charge-coupled device (CCD) camera with 64 × 64 pixels and a 16 × 16 array of lenslets fabricated through the use of binary optics techniques. The sensor measured the wavefront of the beacon radiation arriving from the receiver trailer. The beacon source was a continuous-wave krypton-ion laser ($\lambda = 647$ nm). Because the beacon beam entered the wavefront sensor after reflecting off the deformable mirrors, the wavefront sensor measured only the difference between the actual atmospheric aberrations and the figure on the deformable mirrors. The servo system drove this difference to zero, a mode of operation referred to as null seeking. The frame rate of the wavefront sensor was 1000 Hz, and the maximum system bandwidth was 100 Hz.

Beam-Diagnostic Instrumentation

SABLE included extensive instrumentation, most notably several solid state cameras with high temporal and spatial resolutions, to characterize both the AVM and beacon beams. Table 2 lists the diagnostic measurements and instruments, and Figure 6 shows some of the hardware.

We built an IR wavefront sensor to measure the phasefront of the AVM beam. The sensor was of the Hartmann type with a 32 × 32 lenslet array; the centroids of the focal spots formed by this array were imaged by a 128 × 128 InSb camera. The AVM wavefront shown in Figure 4 was mea-

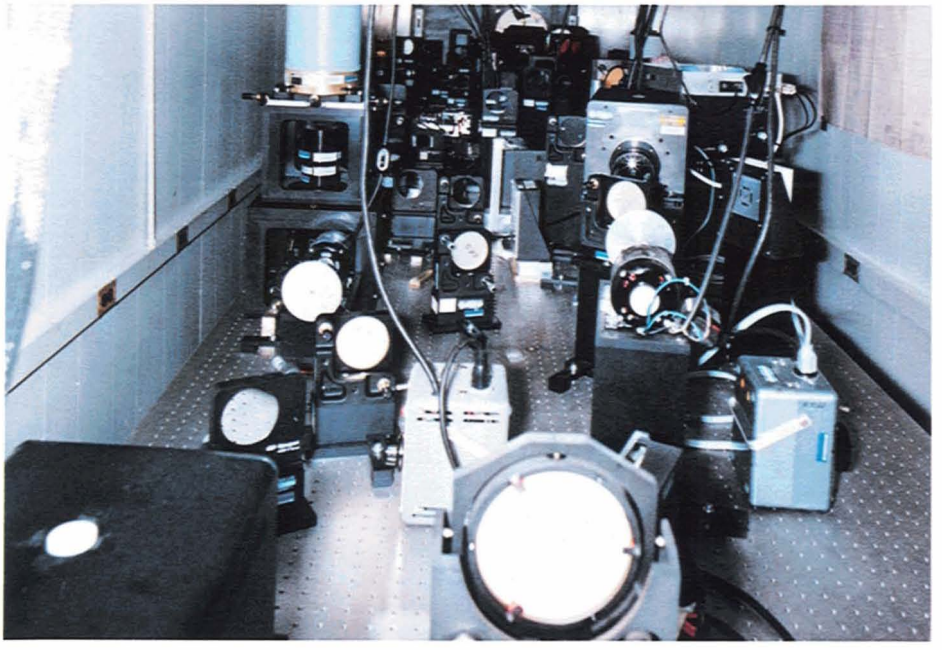

FIGURE 6. Setup in receiver trailer. The AVM beam enters from the far end and is demagnified, split, and imaged to the proper locations for viewing by three cameras. The beacon laser is on a lower level, which is not visible in this photograph. The optical bench is 4' × 10' and full of equipment. In the transmitter building, the optical bench is six times larger and also full of equipment.

sured by this IR sensor.

Recording System

A high-throughput and high-capacity recording system was required to handle the signals from the adaptive optics system and beam-diagnostic instrumentation. We recorded these data on a pair of magnetic disks, each of which accepted up to 9.5 MBytes/sec and had a capacity of 1 GByte. A special-purpose computer with double buffers controlled the transfer of the incoming data streams to the magnetic disks. The recording system was located near the transmitter, and signals from the instruments in the receiver trailer were transmitted to the recording system via high-speed serial optical fibers. At the end of each test day, the data were transferred from the magnetic disks to optical disks for subsequent processing and archiving.

Meteorological Instrumentation

During the experiments, instruments along the propagation path measured characteristics of the atmosphere: wind speed and direction, temperature and velocity turbulence, pressure, temperature, and relative humidity. Towers were used to locate the instruments at the height of the beam and a few meters east (usually downwind) of the actual propagation path (Figure 7).

Propeller anemometers measured the three components of the wind velocity. For the 100-m experiments, the average spacing of the anemometers was about 8 m. For the additional 300 m of the 400-m propagation path, the average spacing was about 13 m. At 50 and 250 m from the transmitter, hot-film anemometers with a 1-kHz bandwidth gathered more detailed information about the temporal and

FIGURE 7. Meteorological instruments on towers. This photograph was taken during preliminary measurements of atmospheric characteristics along the 400-m beam path. For the actual propagation experiments, the towers were much more densely spaced. The beam was propagated to the right (upwind) of the towers at the level of the instruments. For the 400-m tests, the receiver trailer sat on the knoll in the distance.

spatial coherence of the wind field.

The anemometer spacing was chosen as the result of an extensive series of numerical simulations that we had undertaken prior to the propagation experiments. The studies quantified the uncertainty in system performance caused by an incomplete characterization of the wind field. The number of anemometers was chosen to reduce this uncertainty to a level consistent with uncertainties from other sources.

Propagation Ranges

The terrain over which the propagation occurred was marked by hills and valleys. The prevailing winds were generally from west to east during the day, and reversed at night. Suitable values for N_D were attained by propagating the beam from north to south. For most of the 100-m path, the beam was 2 to 4 m above ground. For most of the 400-m path, the beam was 5 to 10 m above ground. Figure 7 provides a sense of the site topography.

Numerical Modeling

The numerical modeling of SABLE under various test conditions was an integral part of the program. Propagation of the high-power beam was modeled with a four-dimensional (x, y, z, and t) computer code called MOLLY [4]. The model permitted the measured characteristics of the laser, atmosphere, and adaptive optics system to be specified in a direct way. For SABLE simulations, the model incorporated the measured characteristics for each spectral line of the AVM—power fraction, irradiance distribution, and atmospheric absorption. Each line was assumed to have the same phase distribution, shown in Figure 4 (right).

The measured wind and turbulence profiles for a particular test were incorporated into the simulation of that test. The time resolution of the meteorological measurements was approximately ½ sec, comparable to a few wind-clearing times.

The temporal and spatial bandwidths of the adaptive optics system were set in the model to correspond to those used during the particular experiment being simulated. The simulations included realistic models of the Hartmann lenslet array and the actual algorithm for wavefront reconstruction from the associated tilt measurements. The measured response function for the deformable mirrors was used to scale the simulated wavefront error signals into actual mirror-figure updates.

An additional feature developed for SABLE was the inclusion of simple response models for the diagnostic cameras. In general, the spatial and temporal bandwidths of the cameras were lower than those used in the code to simulate the interaction of the high-power beam and the atmosphere. By incorporating the response models, we were able to make a more meaningful comparison of code predictions with camera data.

Although MOLLY is a time-dependent code, some temporal details were not included in the SABLE simulations (so that we could save both man-hours in setup time and computer hours in run time). Throughout a code run, the wind field as well as the AVM spectrum and irradiance were held constant. In reality, these quantities did fluctuate somewhat during the few wind-clearing times of an experiment (typically ½ to 1 sec). Also not included in the code simulations were certain imperfections of the experimental system, such as a bad actuator on one of the deformable mirrors. Despite these compromises, there was good agreement between the numerical simulations and the experimental data.

Experimental Results

System performance was generally quite good, as evidenced by well-formed far-field irradiance distributions for the AVM. An example of good system performance is shown in Figure 8. Each picture shows the far-field irradiance distribution of the AVM beam during different stages of a single 400-m test. Figure 8 (top) shows the irradiance early in the test when only 2% of the full AVM power was propagated, so that the blooming was small. At that time, the adaptive optics was compensating mainly for optical turbulence. Figure 8 (middle) shows the irradiance after the adaptive optics system was turned off and an attenuator at the output of the AVM was removed so that the full power of the laser was propagated. Blooming was strong (N_D about 250) and caused considerable spreading of the far-field spot. (Optical turbulence caused only a small fraction of the spread.)

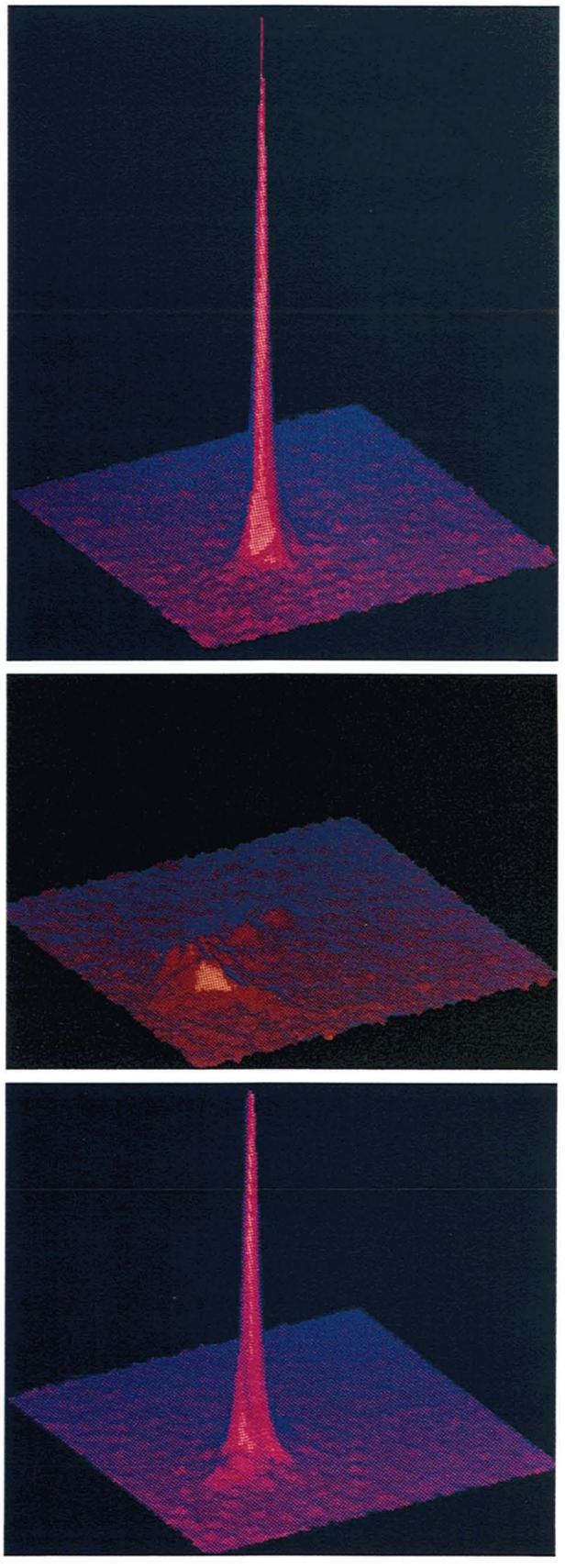

Figure 8 (bottom) shows the same situation as in Figure 8 (middle), except that the adaptive optics had been turned on for a few wind-clearing times, long enough for blooming to equilibrate. The corrected irradiance in Figure 8 (bottom) is similar to that of the no-blooming case in Figure 8 (top), although the peak is not quite so high. Thus the compensation for blooming and turbulence was good, but not perfect.

To help summarize the ensemble of test results, we defined a single-number measure of performance from far-field irradiance distributions such as those in Figure 8. We calculated this dimensionless number, called the relative Strehl ratio, by first dividing the peak irradiance by the total energy to give a measure of the performance independent of the total energy incident on the camera. We then normalized this number by dividing it by the corresponding closed-loop value for the no-blooming reference condition at 2% of the full AVM power. A relative Strehl ratio of unity, therefore, corresponds to perfect correction for distortions due to blooming.

Figure 9 shows scatter plots of relative Strehl ratio versus N_D for many of the 100-m and 400-m tests. Figure 9 (top) shows the data obtained when the adaptive optics system was off. As the blooming strengthens, the relative Strehl ratio decreases rapidly. Figure 9 (bottom) shows the data when the adaptive optics system was on. We see that in general the use of adaptive optics significantly improves system performance, even for N_D as large as 500. The scatter of the data points in Figure 9 is caused mainly by test-to-test variations of other parameters that affect the relative Strehl ratio, such as N_P, σ_v, the level of optical turbulence, and the laser performance.

In Figure 9 (bottom), the relative Strehl ratio generally remains high (≥ 0.5) for N_D up to about 250. In addition, when plotted against N_D divided by N_P

FIGURE 8. Isometric views of far-field irradiance distributions of AVM beam as measured in receiver trailer with charge-coupled device (CCD) camera: (top) $N_D = 5$ with adaptive optics system on, (middle) $N_D = 250$ with adaptive optics system off, and (bottom) $N_D = 250$ with adaptive optics system on. All distributions were measured during the same 400-m laser run with $N_P = 6$, and all three figures have been plotted on the same scale.

(not shown in Figure 9), the relative Strehl ratio generally remains above 0.5 for N_D/N_P up to about 70. These results are favorable because such values for N_D and N_D/N_P are toward the upper limits for currently envisioned ground-to-space systems.

The fairly good system performance up to high values of N_D and N_D/N_P implies that PCI was in general not overwhelmingly important. This conclusion is supported by two other features of the data. First, the decrease in relative Strehl ratio for increasing N_D and N_D/N_P is gradual. In contrast, linearized perturbation theory for PCI (with uniform wind) predicts sudden drastic decreases at some threshold values for N_D and N_D/N_P. Second, system performance was generally best with the maximum number of active actuators (241) and the maximum servo bandwidth (100 Hz), and degraded at lower values. Had PCI been present to a significant degree, performance would have become worse, not better, at higher spatial and temporal bandwidths.

Although PCI was not overwhelming, it did occur in the experiments. Evidence of the presence of PCI was stronger in the 100-m tests, for which N_P and wind variations were relatively low. The measurement showing PCI effects most clearly was that of the beacon irradiance distribution at the image plane between the deformable mirrors. Without atmospheric distortion, the beacon irradiance distribution would have been nearly Gaussian. When the AVM was propagated through the atmosphere with the adaptive optics system turned off, the beacon irradiance distribution generally developed some modulation, especially on the downwind side, in response to the blooming. When the adaptive optics system was turned on, the modulation nearly always became deeper, covered more of the aperture, and aligned more strongly with the wind. Thus feedback effects were clearly evident.

Figure 10(a), taken from the 100-m tests, shows an example of the beacon irradiance distribution with the adaptive optics system turned on. The distribution is strongly modulated with ridges generally parallel to the wind direction. The separation of the ridges corresponds closely to the Nyquist frequency of the adaptive optics system, which, as discussed earlier, is the frequency predicted to have the highest PCI growth rate. The ridges and their direction and spacing are evidence of PCI.

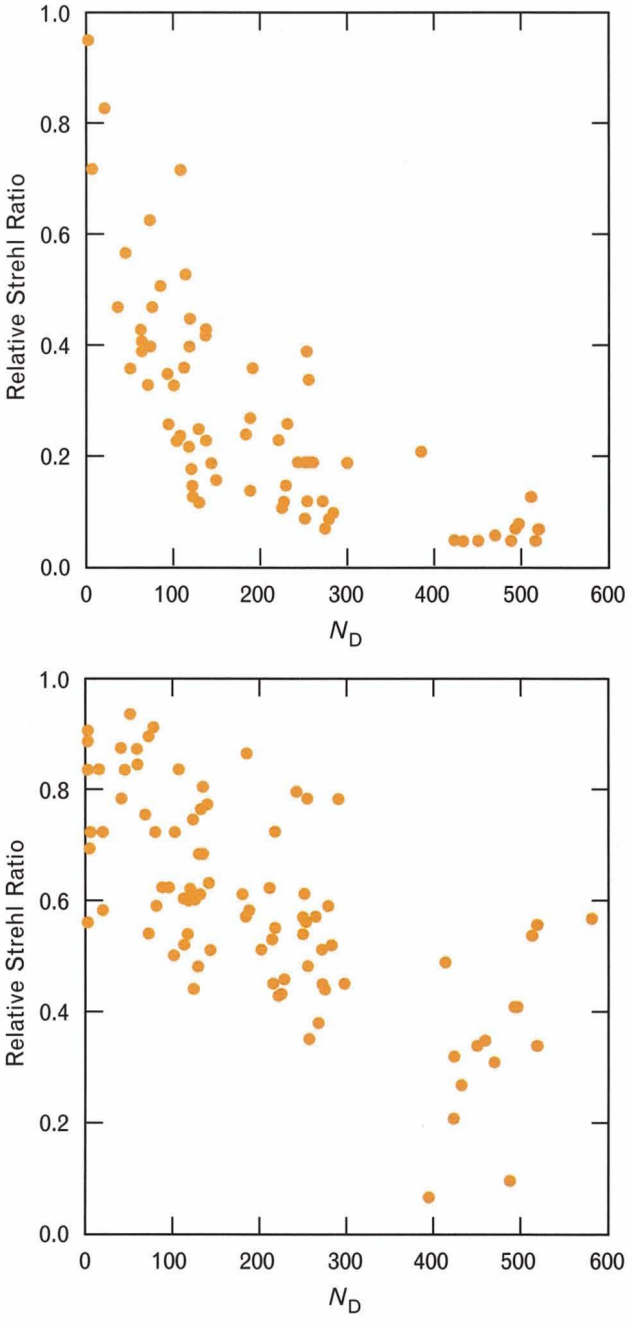

FIGURE 9. Relative Strehl ratio versus N_D: (top) adaptive optics system off, and (bottom) adaptive optics system on. (The relative Strehl ratio is defined in the main text.) The data are from 100-m and 400-m tests with 241 actuators and 100-Hz servo-loop bandwidth.

Figure 10(b) provides an interesting counterpoint and a clue as to why system performance was generally so good. The figure shows the beacon irradiance

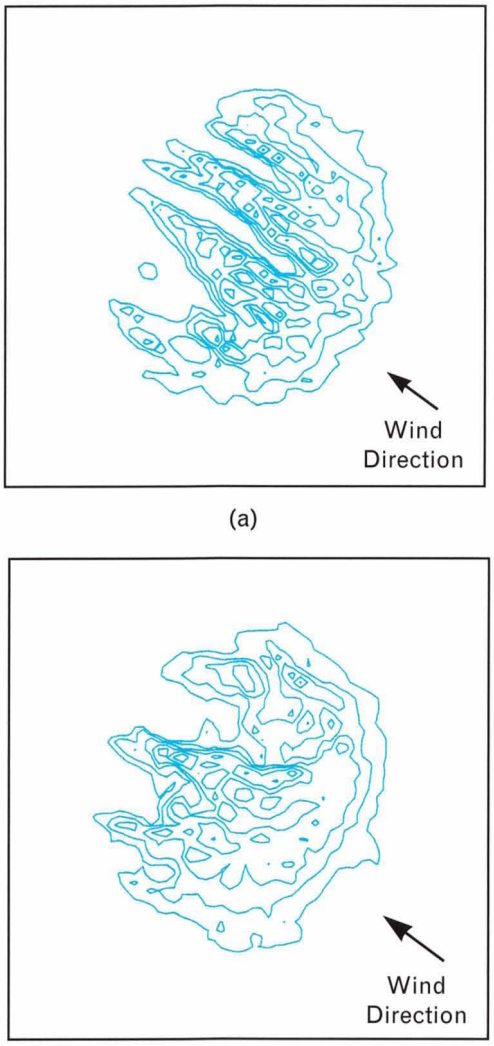

FIGURE 10. Measured beacon irradiance distributions for two 100-m tests. The two tests had similar values for N_D and N_P, but different σ_v: (a) $N_D = 120$, $N_P = 2.5$, and $\sigma_v = 0.25$; and (b) $N_D = 130$, $N_P = 2.5$, and $\sigma_v = 0.45$. The location of the measurement was the image plane between the deformable mirrors.

distribution for another 100-m test with approximately the same values for N_D and N_P, but a higher value for σ_v. We see that the modulation covered less of the aperture, was not so strongly aligned with the wind direction, and was not dominantly at the Nyquist frequency. From Figures 10(a) and 10(b), we conclude that PCI was suppressed by variations in the wind field along the propagation direction.

For the same pair of runs, Figure 11 shows the positive effect of wind variations on the relative Strehl ratio, which is a more direct measure of system performance. The figure shows the relative Strehl ratios versus time, starting at the instant the AVM beam entered the atmosphere. Note that the relative Strehl ratio settled out to a higher value for the case in which the wind variation was larger, even though N_D was actually a little higher for that case. Evidently, even for the 100-m tests, wind variations suppressed PCI and improved system performance significantly.

For the 400-m tests, Nyquist-frequency modulations characteristic of PCI were harder to find. We had expected this result because of the additional wind variations over the longer propagation path. The linearized theory with uniform winds would have predicted significant PCI even with the somewhat higher values of N_P characteristic of the 400-m tests.

For a better understanding of the importance of PCI in the 400-m tests, we looked at the relative Strehl ratios obtained in the deferred adaptive optics mode. In Figure 12, each point represents a 400-m test. The abscissa is the relative Strehl ratio immediately after the adaptive optics was turned on; it shows how much system performance was degraded by

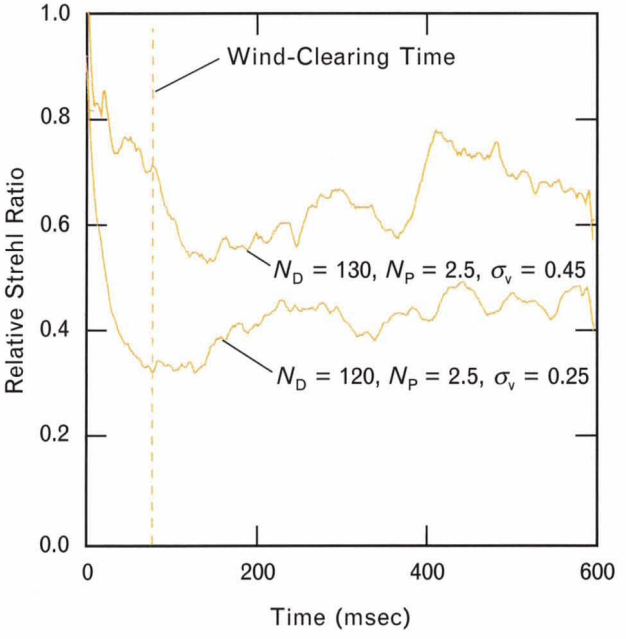

FIGURE 11. Relative Strehl ratios versus time. The data are from the same two 100-m tests as in the previous figure. The two tests had similar values of N_D and N_P, but different σ_v.

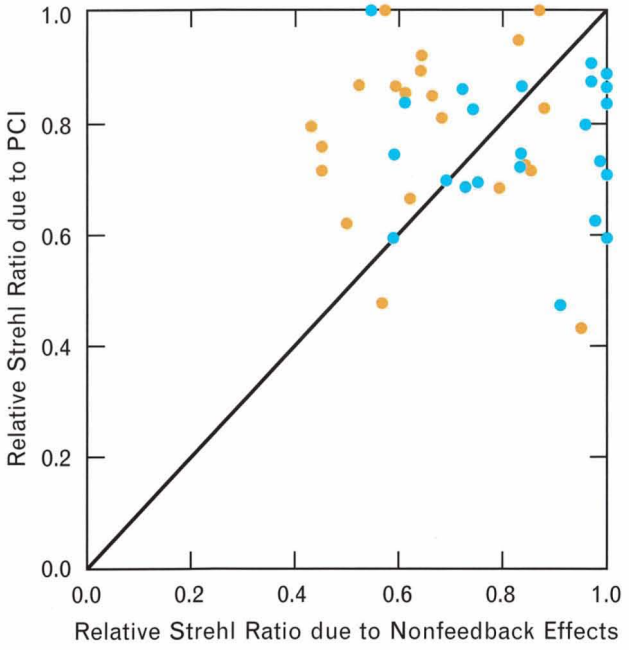

FIGURE 12. Data from deferred adaptive optics tests at 400 m. The abscissa is the relative Strehl ratio just after the adaptive optics loops were closed in the presence of fully developed blooming. Thus the abscissa represents degradation by nonfeedback effects. The ordinate is the additional factor by which the relative Strehl ratio subsequently decayed. Thus the ordinate represents degradation by PCI. The diagonal line represents equal contributions from nonfeedback effects and PCI. Blue points are for tests with $\sigma_v < 0.5$, and tan points for $\sigma_v > 0.5$. The data represent a wide range of N_D.

nonfeedback effects such as fitting error and open-loop thick-lens errors. The ordinate is the additional factor by which the relative Strehl ratio decayed over the few wind-clearing times after the adaptive optics system was turned on; it shows how much system performance was degraded by PCI. (The relative Strehl ratio after a few wind-clearing times is the product of the ordinate and abscissa.) The diagonal line in the figure represents equal contributions from nonfeedback effects and PCI. Points below the diagonal line indicate that PCI caused most of the degradation for those tests; points above the line indicate that most of the degradation was caused by nonfeedback effects.

On the whole, the data points lie as much above as below the diagonal line. Thus PCI was on average no more important than nonfeedback effects. There is, however, a trend associated with the level of wind variations, as indicated by the differences between the tan and blue points. The tan points, which represent tests with a high level of wind variations, tend to lie above the diagonal line, meaning that PCI was less important for these tests. The opposite is true for the blue points. This difference suggests that wind variations suppressed PCI more than they did nonfeedback errors. (The reader may notice that there are more tan points that have low abscissas and may be led to conclude that high wind-variation levels result in poor performance. This conclusion would not be valid. The reason there are more tan points with low abscissas is that near the ground high wind-variation levels often occur when the average wind speed is low. Low average wind speeds result in strong blooming, which limits the Strehl ratio due to nonfeedback effects, such as fitting errors and thick-lens errors.)

In total, the data presented in this section showed that wind variations significantly suppressed PCI and contributed to good system performance in SABLE.

Comparison of Experimental Results with Code Simulations

One of the main objectives of SABLE was to determine how well the numerical model could predict the performance of an adaptive optics system used to compensate for thermal blooming and turbulence in the real atmosphere. In fact, the numerical simulations did agree well with the experimental data across a broad range of operating conditions.

Figure 13, an example from the 400-m tests, compares the measured relative Strehl ratio versus time with the results of computer simulations. The adaptive optics system was on from the beginning of laser propagation; i.e., the ab initio mode of operation was used. At times beyond one wind-clearing time, the data oscillate around an average value because of random temporal variations in the wind field and in the AVM beam coming from the laser. (The code models neither of these random phenomena.)

As indicated in Figure 13, two simulations were run. One used the actual measured wind field, with all its variations in speed and angle, at a particular instant. For this simulation, the value of relative Strehl ratio that was obtained beyond one wind-clearing

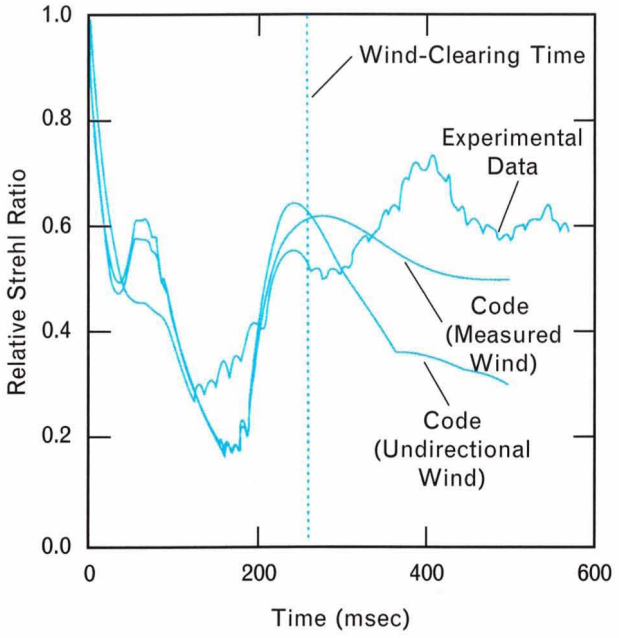

FIGURE 13. Relative Strehl ratio versus time for a 400-m ab initio test with $N_D = 240$, $N_P = 7$, and $\sigma_v = 0.85$. Experimental data and two numerical simulations are shown. One simulation used the measured wind; the other used the same profile of wind speed, but constrained the wind to one direction over the entire propagation path.

time compares well to the time-averaged data. The other simulation, which was run as a computer experiment designed to isolate the importance of wind variations, used the measured wind-speed profile, but constrained the wind to a single direction. By eliminating variations in direction, we expected that the development of irradiance ridges parallel to the wind would be enhanced, and this effect would lead to a degradation in system performance. Figure 13 shows that there was such a degradation. The computer code thus supports the conclusion reached in the previous section that wind variations improve system performance.

The behavior of the relative Strehl ratio in Figure 13 for times less than a wind-clearing time was strongly influenced by an unwanted experimental effect. Each time the fast shutter at the laser opened to start an experiment, the beam pointing direction jittered strongly for a moment. The jitter caused the far-field spot at the camera to move several pixels, and this motion was too rapid for the camera to resolve temporally. Consequently, the camera reported a smeared spot with a lower irradiance than the actual value. The effect, which was very repeatable throughout SABLE, was stronger for the 400-m tests because of the longer range. The jitter was modeled in the code by applying a sinusoidal tilt to the outgoing beam together with an averaging operator to simulate camera smearing. In Figure 13, the strong dip of the relative Strehl ratio between 70 and 200 msec is caused by the jitter. Note that the code models it well.

Figure 14 shows another comparison between experimental data and computer results, this time for a 100-m ab initio test. The data from the high-σ_v case of Figure 11 are repeated here. As before, one simulation used the measured wind field, and the other used the measured speed profile but with a constant direction. These simulations did not include jitter; thus the corresponding curves in Figure 14 do not reproduce the shallow dip evident in the data around 120 msec. For times beyond 200 msec, when jitter had decayed away, the average value of the relative Strehl ratio given by the simulation with the measured wind field

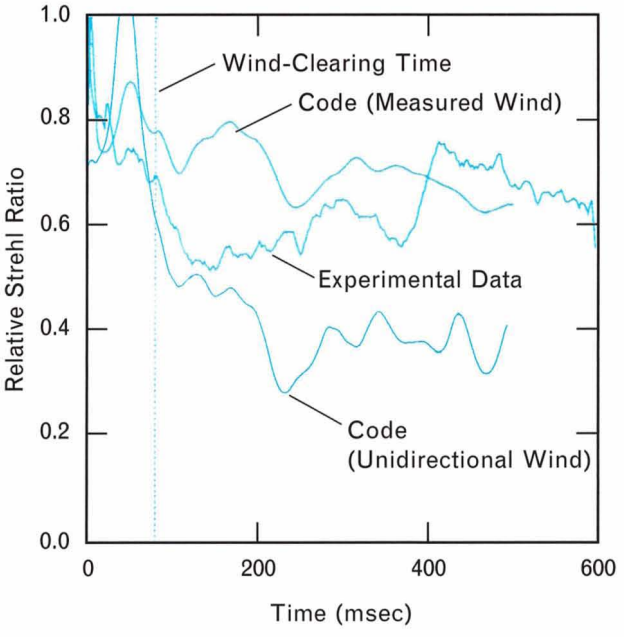

FIGURE 14. Relative Strehl ratio versus time for the 100-m ab initio experiment shown in Figure 11 with $N_D = 130$, $N_P = 2.5$, and $\sigma_v = 0.45$. Experimental data and two numerical simulations are shown. As in Figure 13, one simulation used the measured wind; the other used the same profile of wind speed, but constrained the wind to one direction over the entire propagation path.

agrees relatively well with the observed data. The other simulation, with a unidirectional wind, gives a lower Strehl ratio for times beyond 200 msec. These results provide further evidence that wind variability enhances system performance, a result consistent with the data of Figure 11.

The simulations using a unidirectional wind are examples of the kind of what-if experiments that can be done with the computer model. Having established the validity of the code under actual experimental conditions, we can extend our understanding by numerically exploring the effects of altering various parameters in isolation, an approach that is not practical in field experiments.

The preceding figures have shown that the numerical model can accurately predict system performance in experiments with ab initio adaptive optics. As a somewhat different test of the numerical model, Figure 15 shows the time evolution of the relative Strehl ratio for an experiment with strong thermal blooming (N_D = 220) in which the adaptive optics system was not turned on until after several wind-clearing times; i.e., the deferred mode of operation was used. Note that the simulation faithfully reproduces both the rapid (<50 msec) degradation in performance as the uncorrected blooming developed and the rapid recovery after the adaptive optics system was turned on.

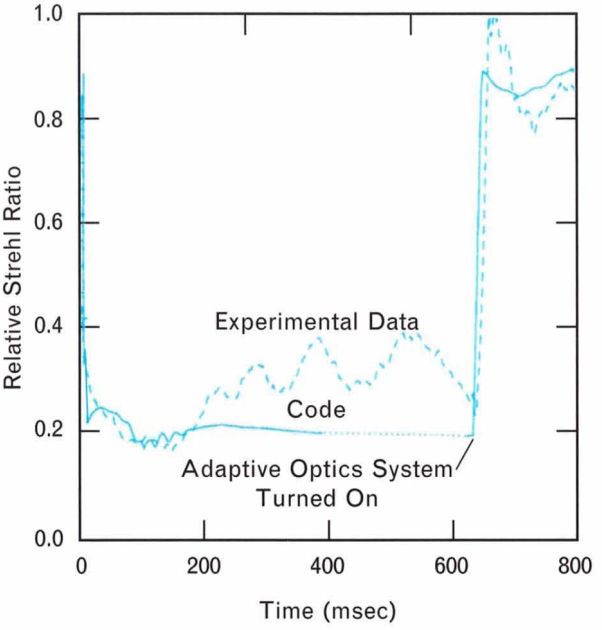

FIGURE 15. Relative Strehl ratio versus time for a 400-m deferred adaptive optics test with N_D = 220, N_P = 7, and σ_v = 0.95. Experimental data and numerical-simulation results are shown. After 400 msec the code results did not change significantly so the 400-msec results were extrapolated to 620 msec and used as initial conditions when the adaptive optics loops were closed.

Summary

The SABLE program fulfilled its three principal objectives. First, phase-conjugate adaptive optics successfully compensated severe blooming in the real atmosphere over a wide range of atmospheric conditions. Second, SABLE demonstrated that real atmospheric wind variations along the propagation path suppressed PCI and significantly improved performance of the system. Third, the computer propagation code accurately modeled system performance for adaptive optics compensation of turbulence and severe blooming in the real atmosphere.

The implications of the SABLE results for a high-power ground-to-space system are favorable. Because of natural variations in the wind field, PCI will usually not be an overwhelming effect, and phase-conjugate adaptive optics can perform adequately. Moreover, although the propagation paths for SABLE were horizontal, we now believe that the code can accurately predict the performance of ground-to-space systems if the wind field is known.

Acknowledgments

SABLE was sponsored by the U.S. Army Strategic Defense Command with funding from the Strategic Defense Initiative Organization. We thank Col. Thomas Meyer, Comdr. Janice Garner, and Albert Carmichael for their interest and support.

The SABLE experiments were reviewed periodically by the Laser Propagation Panel and the JASON study groups. These meetings helped to shape and refine our approach. We acknowledge in particular the insights and guidance offered by David Fried, Frederick Gebhardt, Barry Hogge, Marshall Rosenbluth, and Peter Ulrich.

TRW operated the Alpha Verification Module (AVM), measured its power and spectrum, provided the propagation ranges, and designed and built the new resonator and beam-path conditioning system.

In particular, we thank Charles Kilcline, Gerald Rohles, Donald Bullock, Jeffrey Sollee, Patrick Pomphrey, and Wilhem Behrens.

OptiMetrics, led by Robert Spellicy, Brian Matisse, and Ralph Brewer, put together and operated the meteorological instrumentation. The company was also responsible for recording and processing the meteorological data.

Science Applications International Corporation helped design test plans for the characterization of AVM and made valuable suggestions during the design of the new resonator. In particular, we thank Richard Wade and Jeffrey Dansereau.

At Lincoln Laboratory, our group leader Paul Berger guided the entire effort. Assisting in hardware development were Peter Ford, Keith Serra, Emery Visconti, Herbert Feinstein, Phillip Malyak, and David Hearn. Joseph Bielinski and James Blasi assisted in the integration, installation, and testing of the SABLE system. Staff in the Laser Radar Measurements Group led by Assistant Leader Wilfred Veldkamp provided the binary optics lenslet arrays for the beacon and infrared wavefront sensors. Barry Burke and William McGonagle of the Microelectronics Group developed the charge-coupled device (CCD) camera for the wavefront sensor.

REFERENCES

1. L.C. Bradley and J. Herrmann, "Phase Compensation for Thermal Blooming," *Appl. Opt.* **13**, 331 (1974).
2. D.P. Greenwood and C.A. Primmerman, "Adaptive Optics Research at Lincoln Laboratory," *Linc. Lab. J.* **5**, 3 (1992).
3. D.V. Murphy, "Atmospheric-Turbulence Compensation Experiments Using Cooperative Beacons," *Linc. Lab. J.* **5**, 25 (1992).
4. J.F. Schonfeld, "The Theory of Compensated Laser Propagation through Strong Thermal Blooming," *Linc. Lab. J.* **5**, 131 (1992).
5. J.F. Schonfeld, "Linearized Theory of Thermal-Blooming Phase-Compensation Instability with Realistic Adaptive Optics Geometry," to be published in *J. Opt. Soc. Am. B.*
6. M. Rosenbluth, *Thermal Blooming in the Presence of Wind Shear,* JASON, The MITRE Corp. Report Number JSR-87-926 (McLean, VA, 1990).
7. B. Johnson, "Thermal-Blooming Laboratory Experiments," *Linc. Lab. J.* **5**, 151 (1992).
8. R.J. Briggs, "Models of High-Spatial-Frequency Thermal Blooming Instabilities," *Lawrence Livermore National Laboratory Report UCID-21118* (14 Aug. 1987).
9. P.J. Pomphrey, Jr., D.L. Bullock, G.B. Rohles, D.G. Fouche, J.P. Dansereau, and E.L. Schafer, "Control of Intensity Distribution and Spectra through Resonator Design for the SABLE Propagation Experiments," *Proc. SPIE* **1628**, 176 (1992).
10. H.T. Barclay, P.H. Malyak, W.H. McGonagle, R.K. Reich, G.S. Rowe, and J.C. Twichell, "The SWAT Wavefront Sensor," *Linc. Lab. J.* **5**, 115 (1992).

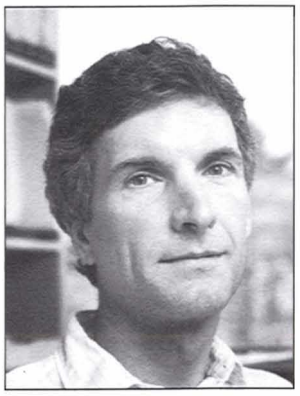

DANIEL G. FOUCHE
was raised in Ohio. He attended Harvard University on an Alfred P. Sloan Scholarship and received a B.A. degree in 1969. He was a National Science Foundation Predoctoral Fellow at Yale University, where he received a Ph.D. in 1972. His thesis topic was on light scattering in molecules. Since joining Lincoln Laboratory in 1972, he has worked mainly in the areas of adaptive optics, laser radar, infrared sensors, and precision tracking.

CHUCK HIGGS
received his undergraduate degree from Miami University, and his master's and doctoral degrees in physics from Rice University. In 1982, he joined Lincoln Laboratory, where his work has been in the areas of nonlinear optics and adaptive optics.

FRED PEARSON
received his undergraduate and master's degrees in Aeronautics and Astronautics from the University of Washington in Seattle. He received a doctorate from Harvard University in the Division of Applied Sciences in 1985. After four years on the Applied Mathematics faculty at MIT, he joined Lincoln Laboratory in 1989. His current research interests include wave propagation, numerical methods, and turbulence.